Available online at www.sciencedirect.com
ScienceDirect
Trans. Nonferrous Met. Soc. China 30(2020) 1524−1534
Transactions of Nonferrous Metals Society of China
www.tnmsc.cn

Fabrication of lotus-type porous Mg−Mn alloys by metal/gas eutectic unidirectional solidification

Can-xu ZHOU[1], Yuan LIU[1,2], Hua-wei ZHANG[1,2], Xiang CHEN[1,2], Yan-xiang LI[1,2]

1. School of Materials Science and Engineering, Tsinghua University, Beijing 100084, China;
2. Key Laboratory for Advanced Materials Processing Technology, Ministry of Education, Tsinghua University, Beijing 100084, China

Received 12 October 2019; accepted 15 April 2020

Abstract: Lotus-type porous Mg–*x*Mn (*x*=0, 1, 2 and 3 wt.%) alloys were fabricated by metal/gas eutectic unidirectional solidification (the Gasar process). The effects of Mn addition and the fabrication process on the porosity, pore diameter and microstructure of the porous Mg−Mn alloy were investigated. Mn addition improved the Mn precipitates and increased the porosity and pore diameter. With increasing hydrogen pressure from 0.1 to 0.6 MPa, the overall porosity of the Mg−2wt.%Mn ingot decreased from 55.3% to 38.4%, and the average pore diameter also decreased from 2465 to 312 μm. Based on a theoretical model of the change in the porosity with the hydrogen pressure, the calculated results were in good agreement with the experimental results. It is shown that this technique is a promising method to fabricate Gasar Mg–Mn alloys with uniform and controllable pore structure.
Key words: porous material; Mg−Mn alloy; porosity; Gasar process; directional solidification

1 Introduction

Magnesium alloys have received intensive attention as a new type of degradable bio-materials [1,2]. The densities, elastic moduli, and stiffness values of magnesium alloys are close to those of human bone [3,4]. Furthermore, porous Mg alloys are promising biodegradable materials for orthopedic applications. These porous biomaterials have been confirmed to facilitate bone ingrowth and may allow for efficient soft tissue attachment to supplement the stability of the implant by biological fixation [5]. However, the poor strength and fatigue resistance of traditional porous materials with randomly distributed pores may dramatically restrict their applications [6]. Compared with traditional porous materials, materials with the lotus-type porous structure prepared by the Gasar technique present less stress concentration around the pores with stress along the longitudinal direction of the pores, and they show excellent mechanical properties [7]. This processing method was first reported by SHAPOVALOV [8] and utilizes the so-called “metal/gas eutectic reaction”, in which the melt is solidified into a solid solution and a gas phase [9−11]. The pore structures of these materials look like lotus roots, so they are also called lotus-type porous materials. Various pure materials and a small amount of alloys have been fabricated into the lotus-type porous structure, such as Cu [12], Mg [7,13], Al [14], Fe [15], Ni [16], Si [17], Al−Cu [18], Al−Ti [19], steel [20], and Cu alloys [21,22]. The pore size and porosity can be controlled by the gas pressure during melting and solidification, the solidification velocity, the temperature during melting, and other parameters [23,24].

Foundation item: Project (51771101) supported by the National Natural Science Foundation of China
Corresponding author: Yuan LIU; Tel: +86-10-62789328; E-mail: yuanliu@tsinghua.edu.cn
DOI: 10.1016/S1003-6326(20)65316-X

Considering the advantages described above, magnesium alloys with the lotus pore structure prepared by Gasar process are the most promising bone implant materials for orthopedic applications. However, pure magnesium has limited clinical application because of its rapid degradation in the body and early failure in chloride-containing solutions, including human body fluids. Therefore, development of magnesium alloys with Zn, Ca, and Mn elements (essential elements to human health) is a research focus of biodegradable metals [1,25]. Researchers have found that small addition of elemental Mn to Mg results in Mg–Mn alloys with good corrosion resistance. GARDEL et al [26] found that up to ~2 wt.% Mn doping can slightly reduce the cathodic kinetics. In addition, GENG et al [27] found that Mg–Mn alloy cervical implants can be used in small animal experiments and proper surface modification can effectively improve the corrosion resistance of the alloy. Mg−Mn alloys can also induce less than 5% hemolysis and reduce the corrosion rate in both SBF (simulated body fluid) and the Hank's solutions [28]. Thus, fabrication and research of Mg−Mn alloys with the lotus-type porous structure can play a great role in development of degradable porous biological magnesium alloys.

Unfortunately, few magnesium alloys have been fabricated by the Gasar process. In this work, lotus-type porous Mg–Mn alloys were fabricated by the Gasar process under various hydrogen pressures. The effects of the alloying element on the porosity and pore size of the lotus-type porous Mg–Mn alloy were investigated. The influence of the hydrogen pressure on the porosity was experimentally and theoretically studied to provide a scientific basis for the fabrication of Gasar biodegradable Mg alloy.

2 Experimental

Lotus-type porous Mg–*x* wt.%Mn (*x*=0, 1, 2 and 3) alloys were fabricated by the Bridgman-type directional solidification method. The chemical compositions of the fabricated Mg alloy ingots are given in Table 1. A schematic diagram of the apparatus used for the Gasar method is shown in Fig. 1. The furnace chamber was separated into a heat zone and a cold zone by a turn-over plate. The copper chiller connected with the dummy bar was in the cold zone, and the mold containing the Mg–Mn alloy was in the heat zone. The alloy was heated under a vacuum degree of 0.05 Pa. After introduction of hydrogen (0.1−0.6 MPa) into the chamber, the melt was held at 700 °C for 2 h to ensure hydrogen saturation (Fig. 1(a)). The turn-over plate was then opened, and the dummy bar rapidly rose up to fetch the mold, and pulled it

Table 1 Chemical compositions of lotus-type porous Mg−*x*Mn alloys

Alloy	Content of element/wt.%	
	Mn	Mg
Mg−1wt.%Mn	0.96	Bal.
Mg−2wt.%Mn	2.18	Bal.
Mg−3wt.%Mn	3.22	Bal.

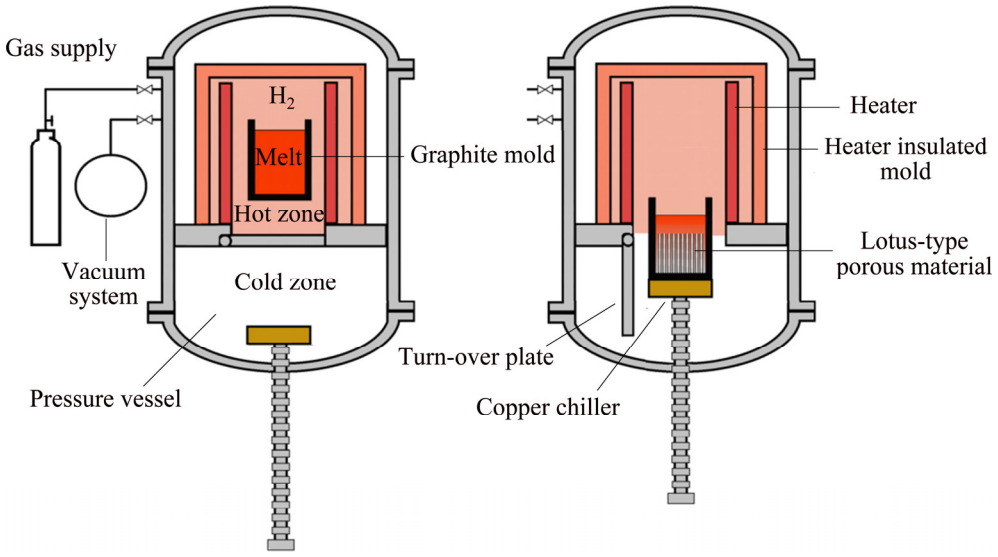

Fig. 1 Schematic diagram of apparatus used for fabrication of Gasar ingot: (a) Heating process; (b) Cooling process

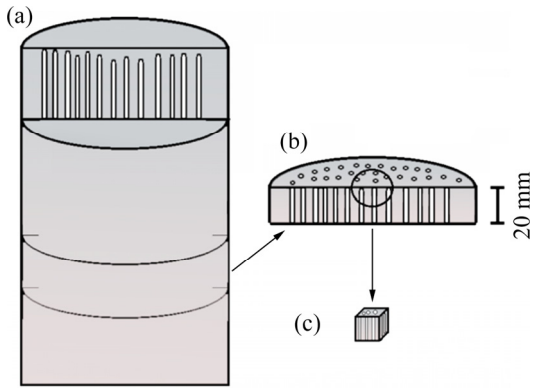

Fig. 2 Schematic diagrams of sampling process: (a) Longitudinal section; (b) Cross-section; (c) Sampling for microstructure observation

down to the cold zone at a drawing speed of 1.5 mm/s (Fig. 1(b)). The ingots obtained were nearly 80 mm in diameter and 80−100 mm in height depending on the porosity. Each cylinder ingot was cut into two parts along the central axis (Fig. 2(a)), and each half cylinder ingot was cut into slices every 20 mm along the longitudinal direction, as shown in Fig. 2(b). A cubic sample (Fig. 2(c)) was cut for the microstructure tests. Each upper surface of the slices was polished with a series of emery papers from 400 to 1000 grits. Subsequently, the slices were successively cleaned with acetone and ethanol in an ultrasonic cleaner. Finally, all of the upper surfaces were scanned with a HP-G3010 scanner. The pore diameter and surface porosity were analyzed with image analysis software. The overall porosity of the entire ingot was evaluated through Archimedes' principle. The preferred orientation of the directionally-solidified sample was analyzed by X-ray diffraction (XRD Bruker D8/Aduance). The microstructures of the specimens were investigated by optical microscopy (Zeiss Axio lmager), scanning electron microscopy (SEM Zeiss GEMINISEM 500), electron probe microanalysis (EPMA JEOL JXA8230) and transmission electron microscopy (TEM Tecnai F30). The samples for SEM and EPMA examination were ground with SiC emery paper up to 4000 grade, and polished with diamond paste down to 1 μm. The samples for optical microscopy examination were etched in 4% Nital solution. The TEM foils were prepared by mechanical thinning and ion-beam technique.

3 Results

3.1 Effect of Mn content on pore structure of Mg−Mn alloy

The morphologies of the Mg–2wt.%Mn alloy on the longitudinal section and cross-section at the middle part of the ingot are shown in Figs. 3(a) and (b), respectively. Mg–Mn alloys with the lotus pore structure were successfully fabricated by the new Gasar apparatus and the whole distribution of pores was approximately homogeneous. Cross-sectional views of the lotus-type porous pure Mg, Mg−1wt.%Mn, Mg−2wt.%Mn and Mg−3wt.%Mn ingots at different heights are shown in Fig. 4. The diameters of the pores were the smallest in porous pure Mg, and coarser pores were found in the Mg−2wt.%Mn alloy ingot. However, with further increasing the Mn content to 3 wt.%, the pore diameter slightly decreased. With increasing height of the ingots, the pores became coarser. The dependences of the surface porosity and average pore diameter on the Mn content of the lotus-type porous Mg–Mn alloys at different heights are shown in Figs. 5(a) and (b), respectively. The pore diameter slightly increased with increasing sample height. As the Mn content increased from 0 to 1, 2 and 3 wt.%, the average pore diameter increased from 216 to 258, 312 μm and then decreased from 312 to 302 μm, respectively. The surface porosity first increased then decreased with increasing Mn addition. Similar to the surface porosity, as the Mn content increased from 0 to 1, 2 and 3 wt.%, the overall porosity of the ingots increased from 36.2% to 36.9%, 38.4%, and then decreased from 38.4% to 37.5%.

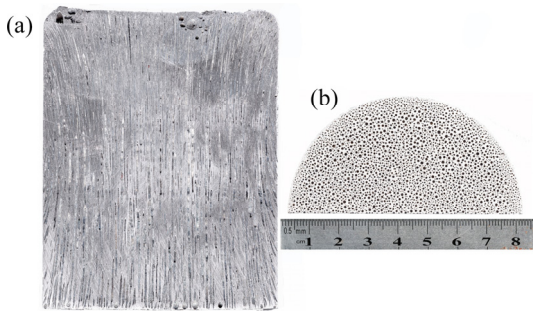

Fig. 3 Pore morphologies on longitudinal section (a) and cross-section (b) at middle part of fabricated Gasar Mg−2wt.%Mn alloy ingot (T=700 °C, $P(H_2)$=0.6 MPa)

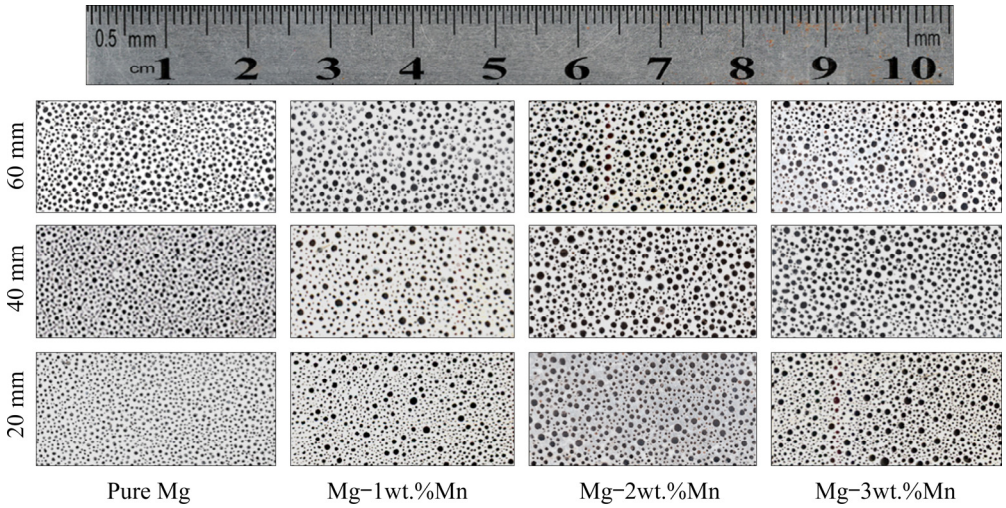

Fig. 4 Pore morphologies of transversal sections of ingots with different Mn contents at different heights

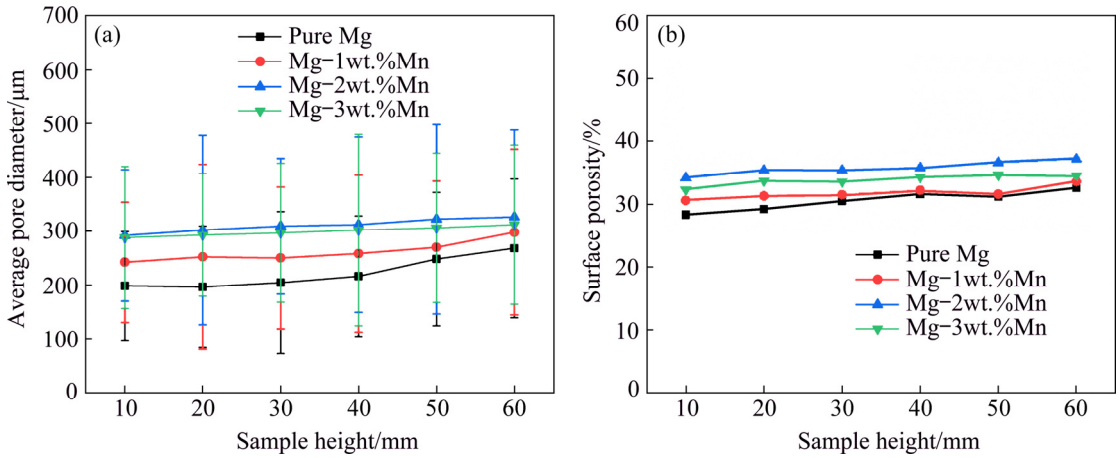

Fig. 5 Comparison of average pore diameter (a) and surface porosity (b) of ingots with different Mn contents at different heights

XRD patterns of the cross-section perpendicular to the solidification direction for the pure Mg, Mg−1wt.%Mn, Mg−2wt.%Mn and Mg−3wt.%Mn ingots are shown in Fig. 6. For pure Mg, the $(11\bar{2}2)$ peak was higher than the other peaks, which indicates that the normal direction of the $(11\bar{2}2)$ planes was preferentially orientated along the solidification direction. Similarly, the preferentially orientated directions of Mg–1wt.%Mn, Mg–2wt.%Mn and Mg–3wt.%Mn were the normal directions of the $(10\bar{1}3)$, $(10\bar{1}3)$ and $(10\bar{1}2)$ planes, respectively, which indicates that the addition of Mn affects the pore structure and grain growth. Optical microscopy images of the microstructure parallel to the solidification direction for the porous Mg–3wt.%Mn alloys are shown in Fig. 7. Coarse precipitates were found in the grains and the sizes were several micrometers (Fig. 7(a)).

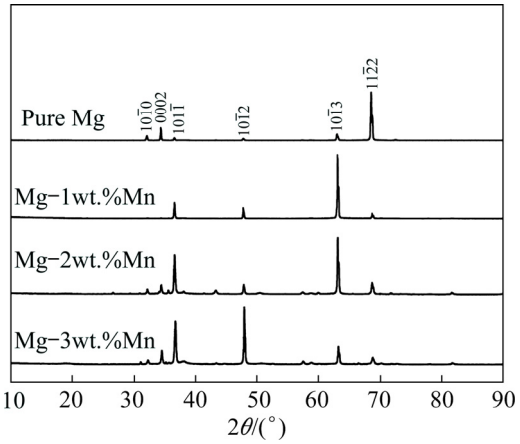

Fig. 6 XRD patterns of pure Mg and Mg−Mn alloys

Fine precipitates were also found along the boundary (area circled in Fig. 7(b)), and a pore was found near this boundary. There were also some precipitates near the end of the pore (Fig. 7(c)),

which indicates that these precipitates can affect the nucleation of the pores. The element distribution of the porous Mg–3wt.%Mn alloy determined by EPMA is shown in Fig. 8. The precipitates along the boundary and in the grain had similar compositions. They were rich in Mn and barely contained any Mg element, and they were considered to be α-Mn.

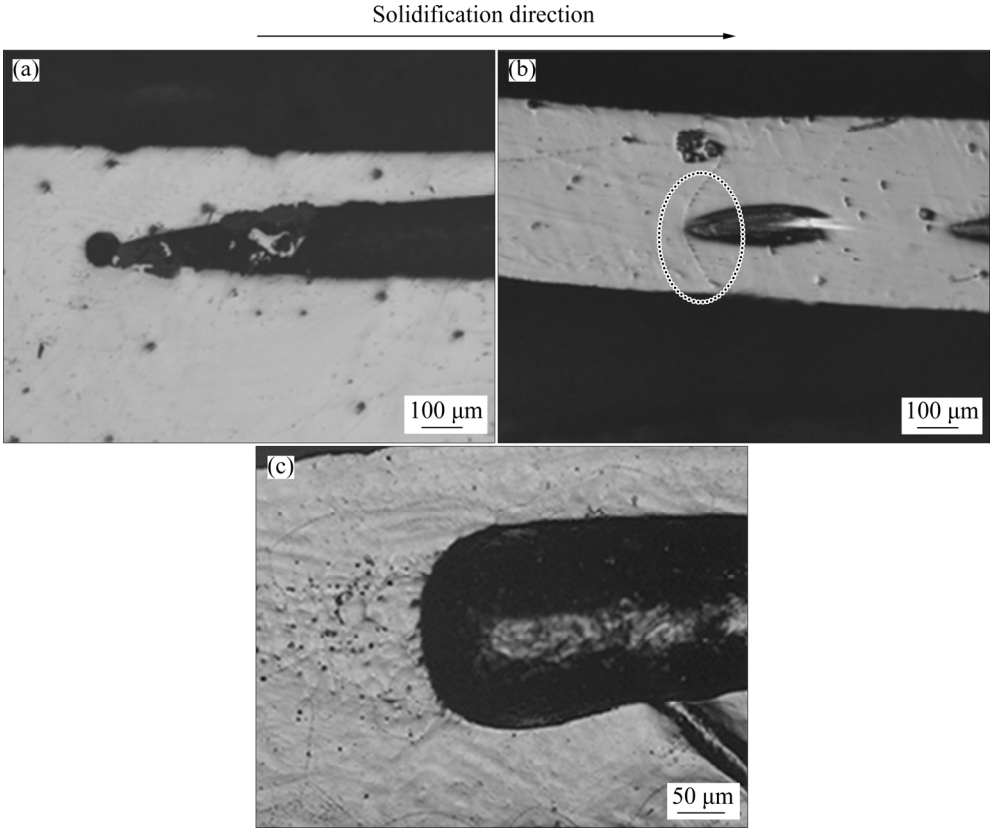

Fig. 7 Optical microscopy images of microstructure parallel to solidification direction for porous Mg−3wt.%Mn alloys: (a) Coarse precipitates in grains; (b) Fine precipitates along boundary; (c) Precipitates at end of pore

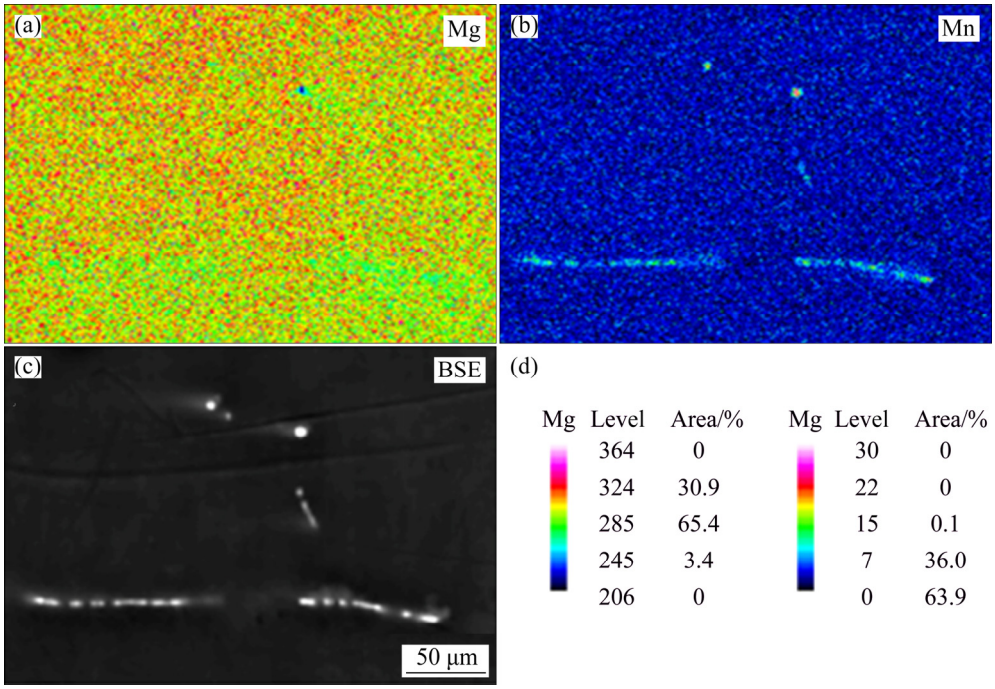

Fig. 8 Element distributions of porous Mg−3wt.%Mn alloys determined by EPMA

3.2 Effects of H_2 pressure on pore structure of Mg−Mn alloys

The typical pore morphologies at different heights for lotus-type porous Mg−2wt.%Mn ingots produced with different H_2 pressures are shown in Fig. 9. The average pore diameter decreased with increasing hydrogen pressure. Similar to Fig. 4, the pore diameter slightly increased with increasing sample height. The dependences of the surface porosity and average pore diameter on the hydrogen pressure for lotus-type porous Mg−2wt.%Mn specimens fabricated at a melt holding temperature of 700 °C are shown in Figs. 10(a) and (b). Increasing the hydrogen pressure decreased the porosity and average pore diameter. When the hydrogen pressure increased from 0.1 to 0.2, 0.4 and 0.6 MPa, the overall porosity changed from 55.3% to 49.6%, 42.6% and 38.4%, and the average pore diameters decreased from 2465 to 1222, 598 and 312 μm, respectively.

3.3 Effect of formation of pores on microstructure of Mg−2wt.%Mn alloy

To further investigate the effect of the pores on the microstructure of the Mg−2wt.%Mn alloy, the nonporous Mg−2wt.%Mn alloy was fabricated by the same process (melt temperature of 700 °C and drawing speed of 1.5 mm/s) for comparison. The microstructures of longitudinal sections of the nonporous and porous Mg−2wt.%Mn alloys are shown in Figs. 11(a) and (b), respectively. The size of the columnar grains was larger in the nonporous Mg−2wt.%Mn alloy than in the porous Mg−2wt.%Mn alloy. For the porous Mg−2wt.%Mn alloy, fine grains with width less than 100 μm were found near the pore area. The grains nucleated at the pore wall, rapidly grew into the nearest melt, and gradually bent to grow along the solidification

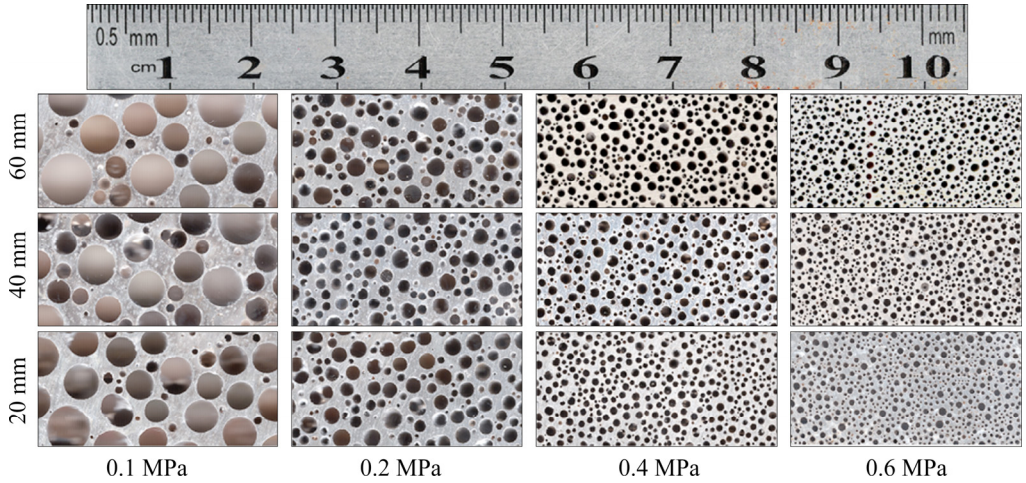

Fig. 9 Pore morphologies of transversal sections at different heights for Mg−2wt.%Mn ingots fabricated with different hydrogen pressures

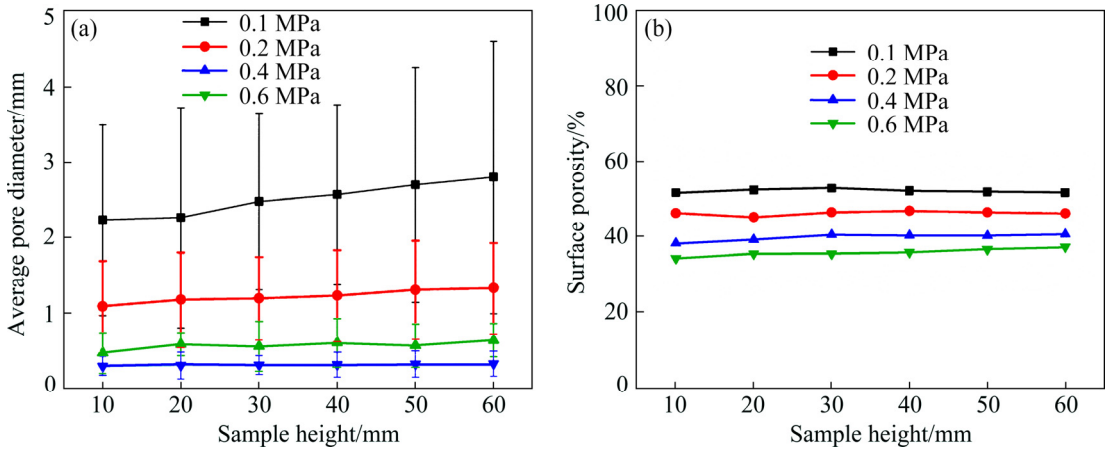

Fig. 10 Comparison of average pore diameter (a) and surface porosity (b) of ingots at different heights produced with different hydrogen pressures

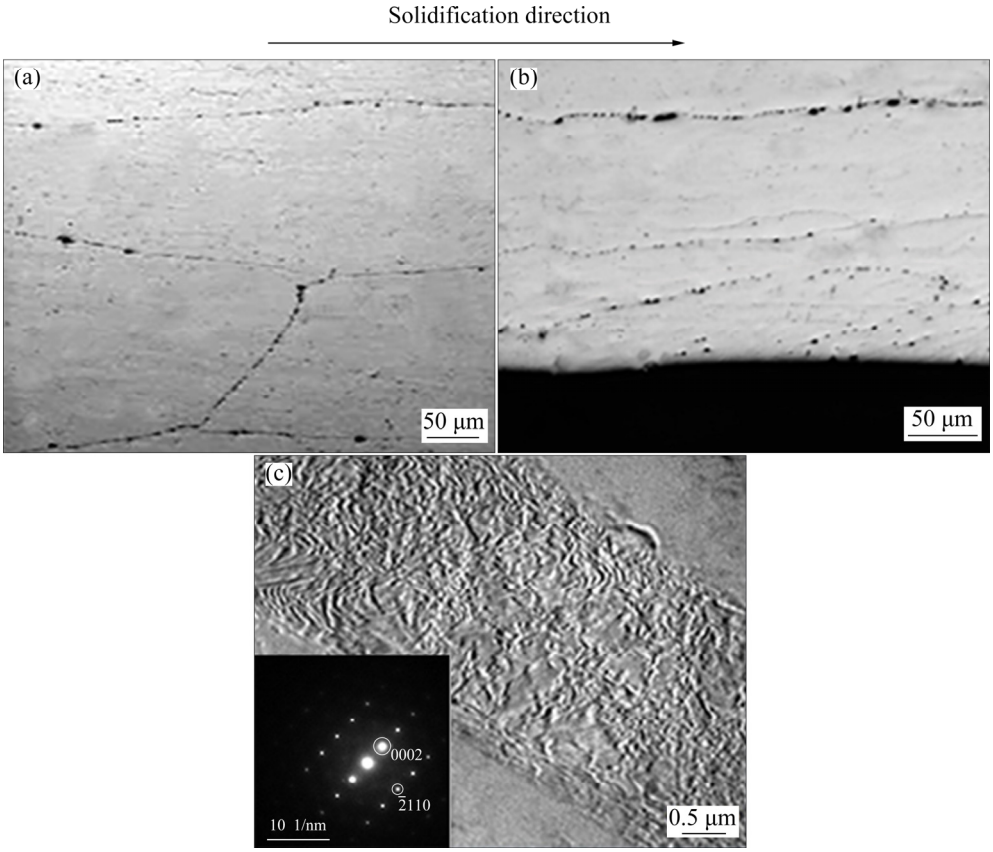

Fig. 11 Optical microscopy images of microstructure parallel to solidification direction in nonporous (a) and porous (b) Mg−2wt.%Mn alloys and TEM bright field image near pore area of porous Mg−2wt.%Mn alloy (c)

direction. A TEM images of the porous Mg–2wt.%Mn alloys near the pore area is shown in Fig. 11(c). And very fine grain with width of nearly 3 μm was found in the alloy and the selected area electron diffraction pattern showed that this grain was the α-Mg phase (beam direction $[01\bar{1}0]$).

4 Discussion

4.1 Effect of Mn content on pore structure of Mg−Mn ingots

Figure 12(a) shows that the solubility of H_2 in the Mg–Mn melt at 700 °C linearly increases with increasing Mn content [29]. In general, more H_2 dissolved in the melt leads to higher porosity. However, in this work, the porosity of the Mg–Mn alloy did not significantly increase when the Mn content was above 2 wt.%. Mg–Mn phase diagram in the Mg-rich corner is shown in Fig. 12(b) [30]. The first equilibrium is a peritectic reaction at 651 °C, and the solubility of Mn in the Mg matrix at this temperature is 2.2 wt.%. When the content of Mn increases to, for example 3 wt.%, the excessive Mn exists as β-Mn (above 700 °C) or α-Mn in the liquid Mg–Mn melt. More solid Mn in the Mg melt may increase the number of bubble nucleation sites, which can lead to escape of the bubbles during the melt cooling process. Thus, the porosity decreased when the Mn content increased to 3 wt.%. ONISHI et al [16] and KASHIHARA et al [31] found that addition of NiO powder, as a form of inclusion, can increase the number of nucleation sites and the insoluble hydrogen may be trapped by these sites, which can increase the porosity. However, in this work, more Mn solid in the Mg matrix did not significantly increase the porosity. It is known that precipitation of α-Mn in Mg, which is different from inclusion of NiO, shows less defects (pits and cracks) at the interface, and there is a coherent interface relationship between Mg and α-Mn with $(10\bar{1}0)_{Mg}//(301)_{Mn}$ and $[\bar{1}2\bar{1}6]_{Mg}//[1\bar{2}\bar{3}]_{Mn}$ [32], so less insoluble hydrogen can be trapped.

With the increasing of doping amount of Mn, the thermal conductivity of Mg−Mn alloy decreases, which can decrease the solidification speed and increase the pore diameter. When the Mn content is

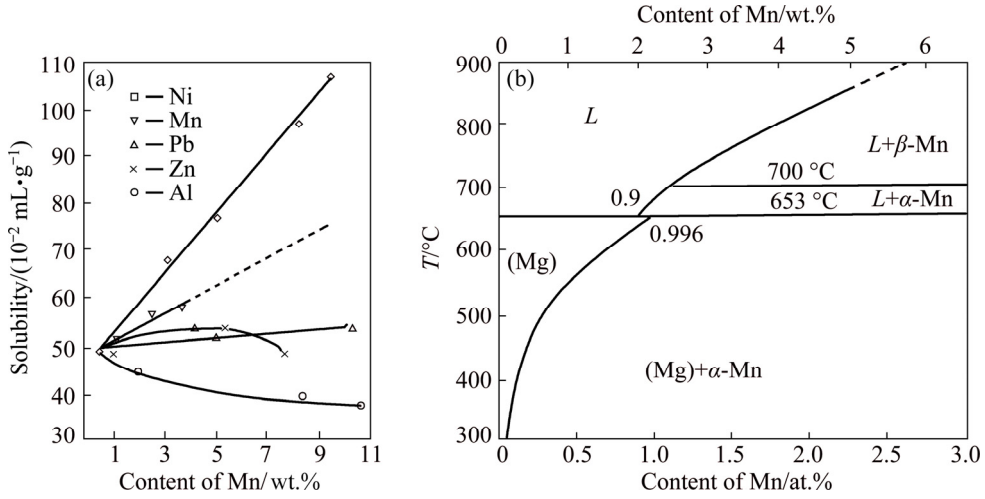

Fig. 12 Effects of alloying elements on solubility of hydrogen in Mg at 700 °C [29] (a) and Mg-rich corner of Mg−Mn phase diagram [30] (b)

below 2.2 wt.%, Mn exists as a solid solution in the melt at 700 °C, and as the Mn content reaches 3 wt.%, besides the solid solution, more α-Mn or β-Mn can precipitate from the melt. Usually, the precipitates have less effect on the thermal conductivity than the solid solution, and the decreasing degree of the thermal conductivity is reduced as the Mn content further increases from 2.2 wt.%. In addition, more Mn as precipitates in the melt may increase the number of pore nucleation sites and may lead to the decrease in the average pore diameter, which is similar to the effect of NiO on the pore diameter in lotus-type porous nickel [16].

4.2 Prediction of porosity of Mg−2wt.%Mn fabricated with different H_2 pressures

It is known that the porosity is an important parameter, and it is sensitive to the pressure. LIU et al [9] successfully predicted the porosity by a theoretical model of Mg/H_2:

$$\varepsilon=\frac{[C_0(1-\alpha)\rho_s-\bar{C}_s\rho_l]RT_m}{[C_0(1-\alpha)\rho_s-\bar{C}_s\rho_l]RT_m+P_{pore}\rho_l} \quad (1)$$

where ε is the theoretical overall porosity, R is the gas constant, T_m is the melting point of the metal, P_{pore} is the gas pressure in the pore, which is almost equal to the furnace atmosphere, C_0 is the initial hydrogen concentration in the liquid metal, C_s is the hydrogen concentration in the solid metal, ρ_s and ρ_l are the densities of the solid and liquid metal near the temperature of melting point, and α is the escape coefficient, which is equal to the ratio of the escaping hydrogen and the original hydrogen concentration in the liquid metal. In this work, C_0 and C_s are the initial hydrogen concentrations in the liquid and solid Mg–2wt.%Mn alloy, respectively. The mole fraction of hydrogen in the alloy, x_H, can be determined by the following equation [21]:

$$\ln X_H=\sum_i x_i \ln x_{H,i}+\Delta G_m^{ex}/(RT) \quad (2)$$

where x_H is the mole fraction of hydrogen in the alloy, x_i is the mole fraction of alloying element i in the alloy, $x_{H,i}$ is the mole fraction of the hydrogen in the pure element i, and ΔG_m^{ex} is the excessive molar Gibbs free energy. The solubilities of hydrogen in the liquid and solid pure element Mg/Mn, $S_{H,Mg/Mn}$, are expressed by the following equations [33]:

$$\ln S_{H,Mg}=6.558-\frac{2533}{T}+\frac{1}{2}\ln\left(\frac{P(H_2)}{P_0}\right) \text{ (liquid)} \quad (3)$$

$$\ln S_{H,Mg}=5.701-\frac{2210}{T}+\frac{1}{2}\ln\left(\frac{P(H_2)}{P_0}\right) \text{(solid)} \quad (4)$$

$$\ln S_{H,Mn}=5.415-\frac{2045}{T}+\frac{1}{2}\ln\left(\frac{P(H_2)}{P_0}\right) \text{(liquid)} \quad (5)$$

$$\ln S_{H,Mn}=4.553-\frac{1378}{T}+\frac{1}{2}\ln\left(\frac{P(H_2)}{P_0}\right) \text{(solid)} \quad (6)$$

And ΔG_m^{ex} can be expressed as follows:

$$\Delta G_{\mathrm{m}}^{\mathrm{ex}} = x_i x_j L_{i,j} \quad (7)$$

$L_{i,j}$ is the Redlich–Kister parameter. For Mg–Mn binary alloy [34]:

$$L_{\mathrm{Mg,Mn}}^{0,\mathrm{liquid}} = 25922.4 + 9.0357T \quad (8)$$

$$L_{\mathrm{Mg,Mn}}^{1,\mathrm{liquid}} = -3470.8 \quad (9)$$

$$L_{\mathrm{Mg,Mn}}^{0,\mathrm{HCP}} = 37148.1 - 1.8103T \quad (10)$$

The density of the Mg–2wt.%Mn alloy was calculated by the linear addition principle. The predicted porosity values of Mg–2wt.%Mn alloys with different hydrogen pressures were in good agreement with the experimental values (Table 2).

Table 2 Comparison of calculated porosities and experimental values from hydrogen pressure effect on porosity of Mg−2wt.%Mn alloy

Hydrogen pressure/MPa	Experimental porosity/%	Calculated porosity/%
0.1	55.3	61.2
0.2	49.6	53.7
0.4	42.6	44.6
0.6	38.4	39.2

Melting temperature: 700 °C; withdraw speeding: 1.5 mm/s

4.3 Effect of pores on microstructure of Mg–2wt.%Mn alloy

In this work, microstructural evolution in the porous material was different from that in the nonporous material. In the porous alloys, the grains near the pore were finer than those in other areas, and the growth direction of the grains was deflected. This indicated that hydrogen bubbles can influence grain nucleation in the Mg–Mn alloys. In addition, the deflection of the crystalline lattice resulted from the different temperatures near the bubble area and inside the melt, and this temperature gradient can influence the growth of the crystal.

Based on the above results, a model for pore formation in the Mg–Mn alloys is schematically illustrated in Fig. 13. The existence of the Mn phase in the melt can provide nucleation sites for pores (hydrogen bubble, circle area 1), and the formation of the pore in the melt also influences nucleation and growth of Mg−Mn grains (circle area 2). Thus, the Mg–Mn alloy fabricated by the Gasar process shows a unique pore structure and microstructure.

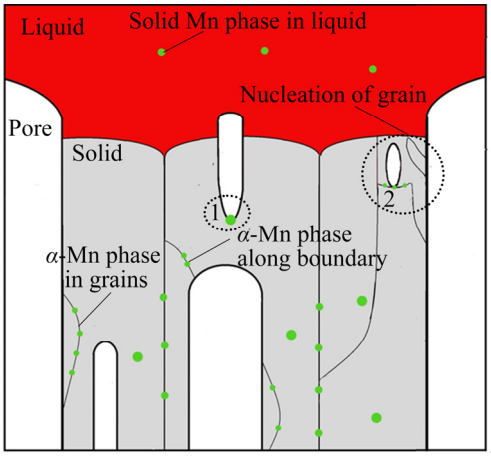

Fig. 13 Schematic illustration of pore formation in Mg–Mn alloy during cooling process

5 Conclusions

(1) As the content of Mn increased from 0 to 2 wt.%, the overall porosity of the ingot increased from 36.2% to 38.4%, and the overall porosity decreased from 38.4% to 37.5% when the Mn content further increased to 3 wt.%. The average pore diameter increased from 216 to 258 and 312 μm, and then decreased to 302 μm when the Mn content increased from 0 to 1, 2 and 3 wt.%, respectively. The α-Mn phase can precipitate in the grains or along the grain boundaries.

(2) With increasing of hydrogen pressure from 0.1 to 0.6 MPa, lotus-type porous Mg–2wt.%Mn alloys with porosities from 55.3% to 38.4% and average pore diameters from 2465 to 312 μm were fabricated with a melting temperature of 700 °C and a withdraw speed of 1.5 mm/s. The calculated porosity changing with the hydrogen pressure agreed well with the experimental results.

(3) Addition of Mn had a significant effect on the pore structure and grain growth. Compared with the nonporous Mg–2wt.%Mn alloy, the size of grains decreased in the porous Mg–2wt.% Mn alloy and more fine grains were found near the pore area.

References

[1] GU Xue-nan, ZHENG Yu-feng. A review on magnesium alloys as biodegradable materials [J]. Frontiers of Materials Science in China, 2010, 4: 111−115.

[2] WU Shu-xu, WANG Shou-ren, WANG Gao-qi, YU Xiu-chun, LIU Wen-tao, CHANG Zheng-qi, WEN Dao-sheng. Microstructure, mechanical and corrosion properties of magnesium alloy bone plate treated by

high-energy shot peening [J]. Transactions of Nonferrous Metals Society of China, 2019, 29: 1641−1652.

[3] SEZER N, EVIS Z, KAYHAN S M. Review of magnesium-based biomaterials and their applications [J]. Journal of Magnesium and Alloys, 2018, 6(1): 23−43.

[4] SALLEH E M, ZUHAILAWATI H, RAMAKRISHNAN S. Synthesis of biodegradable Mg−Zn alloy by mechanical alloying: Statistical prediction of elastic modulus and mass loss using fractional factorial design [J]. Transactions of Nonferrous Metals Society of China, 2018, 28: 687−699.

[5] VAHID A, HODGSON P, LI Yun-cang. New porous Mg composites for bone implants [J]. Journal of Alloys and Compounds, 2017, 724: 176−186.

[6] KOHN D H , DUCHEYNE P. A parametric study of the factors affecting the fatigue strength of porous coated Ti−6A1−4V implant alloy [J]. Journal of Biomedical Materials Research, 1990, 24: 1483−1501.

[7] TANE M, MAYAMA T, ODA A, NAKAJIMA H. Effect of crystallographic texture on mechanical properties in porous magnesium with oriented cylindrical pores [J]. Acta Materialia, 2015, 84: 80−94

[8] SHAPOVALOV V I. Method of manufacture of porous articles: U.S. Patent, 5189549 [P]. 1993−01−26.

[9] LIU Yuan, LI Yan-xiang, WAN Jiang, ZHANG Huang-wei. Evaluation of porosity in lotus-type porous magnesium fabricated by metal/gas eutectic unidirectional solidification [J]. Materials Science and Engineering A, 2005, 402: 47−54.

[10] NAKAJIMA H, HYUN S K , OHASHI K. Fabrication of porous copper by unidirectional solidification under hydrogen and its properties [J]. Colloids and Surfaces A: Physicochemical and Engineering Aspects, 2001, 179: 209−214.

[11] LIU Yuan, LI Yan-xiang. Theoretical analysis of bubble nucleation in GASAR materials [J]. Transactions of Nonferrous Metals Society of China, 2003, 13: 830−834.

[12] CHEN Liu-tao, ZHANG Hua-wei, LIU Yuan, LI Yan-xiang. Experimental research on heat transfer performance of directionally solidified porous copper heat sink [J]. Acta Metallurgica Sinica, 2012, 48(3): 329−323. (in Chinese)

[13] LIU Yuan, LI Yan-xiang, ZHANG Huang-wei, WAN Jiang. Effect of Gasar processing parameters on structure of lotus-type porous magnesium [J]. Rare Metal Materials and Engineering, 2005, 34(7): 1128−1130. (in Chinese)

[14] LIU Xiao-bang, LI Yan-xiang, HE Yun. Fabrication of high-porosity lotus-type porous aluminum in vacuum [J]. Metallurgical and Materials Transactions A, 2017, 48: 1264−1272.

[15] HYUN S K, UCHIKOSHI M, MIMURA K, ISSHIKI M, NAKAJIMA H. Fabrication of porous high-purity iron with directional pores by continuous zone melting technique [J]. Materials Transactions, 2010, 51: 2076−2079.

[16] ONISHI H, UENO S, NAKAJIMA H. An effect of addition of NiO powder on pore formation in lotus-type porous nickel [J]. Materials Transactions, 2008, 49: 2670−2672.

[17] YANG Qian-qian, LIU Yuan, LI Yan-xiang, ZHANG Yan. Pore structure of unidirectional solidified lotus-type porous silicon [J]. Transactions of Nonferrous Metals Society of China, 2014, 24: 3517−3523.

[18] SUZUKI S, KIM T B, NAKAJIMA H. Fabrication of Al−Cu alloy with elongated pores by continuous casting technique [J]. Journal of Physics: Conference Series, 2009, 165: 012068.

[19] KIM T B, TANE M, SUZUKI S, NAKAJIMA H. Pore morphology of porous Al−Ti alloy fabricated by continuous casting in hydrogen atmosphere [J]. Materials Transactions, 2010, 51: 1871−1877.

[20] IKEDA T, AOKI T, NAKAJIMA H. Fabrication of lotus-type porous stainless steel by continuous zone melting technique and mechanical property [J]. Metallurgical and Materials Transactions A, 2005, 36: 77−86.

[21] JIANG Guang-rui, LI Yan-xiang, LIU Yuan. Influence of solidification mode on pore structure of directionally solidified porous Cu−Mn alloy [J]. Transactions of Nonferrous Metals Society of China, 2011, 21: 88−95.

[22] KIM Sang-Wook, LEE Ji-Woon, JUNG Taek-Kyun, HYUN Soong-Keun. Effect of alloying elements on pore characteristics of lotus-type porous Cu−X alloys (X = Ni, Co, Mn, Si, Sn, P) [J]. Materials Characterization, 2017, 123: 99−105.

[23] LIU Yuan, LI Yan-xiang, LIU Run-fa, ZHOU Rong, JIANG Ye-hua, LI Zhen-hua. Theoretical analysis on effect of transference velocity on structure of porous metals fabricated by continuous casting Gasar [J]. Acta Metallurgica Sinica, 2010, 46(2):129−134. (in Chinese)

[24] ZHANG Huang-wei, LI Yan-xiang, LIU Yuan. Gas pressure condition for obtaining uniform lotus-type porous structure by Gasar process [J]. Acta Metallurgica Sinica, 2006, 42(11): 1171−1176. (in Chinese)

[25] BAKHSHESHI-RAD H R, DAYAGHI E, ISMAIL A F, AZIZ M, AKHAVAN-FARID A, CHEN Xiong-biao. Synthesis and in-vitro characterization of biodegradable porous magnesium-based scaffolds containing silver for bone tissue engineering [J]. Transactions of Nonferrous Metals Society of China, 2019, 29: 984−996.

[26] GANDEL D S, EASTON M A, GIBSON M A, BIRBILIS N. Influence of Mn and Zr on the corrosion of Al-free Mg alloys: Part 2 — Impact of Mn and Zr on Mg alloy electrochemistry and corrosion [J]. Corrosion , 2013: 69(8): 744−751.

[27] GENG Fang, JIANG Ming-wei, XIA Tian. Development and feasibility of Mg−Mn alloy cervical implant for small animal experiments [J]. Orthopaedic Biomechanics Materials and Clinical Study, 2016, 13: 5−8. (in Chinese)

[28] GU Xue-nan, ZHENG Yu-feng, CHENG Yan, ZHONG Sheng-ping, XI Ting-fei. In vitro corrosion and biocompatibility of binary magnesium alloys [J]. Biomaterials, 2009, 30: 484−498.

[29] WATANABE T. Hydrogen in magnesium and its alloys [J]. Journal of the Faculty of Liberal Arts, 1974, 5: 47−55.

[30] MANCHESTER F D. Phase diagrams of binary hydrogen alloys [M]. Materials Park: ASM International, 2000.

[31] KASHIHARA M, YONETANI H, SUZUKI S, NAKAJIMA H. Effect of addition of NiO powder on pore formation in lotus-type porous carbon steel fabricated by continuous casting [J]. Materials Science Forum, 2010, 658: 215−219.

[32] ZHANG Ding-fei, SHI Guo-liang, ZHAO Xia-bing, QI

Fu-gang. The evolution and effect of Mn element in Mg−Zn−Mn Alloy [J]. Material Review, 2011, 25(9): 1−5. (in Chinese)

[33] ZHANG Huang-wei, LI Yan-xiang, LIU Yuan. Hydrogen solubility in pure metals for Gasar process [J]. Acta Metallurgica Sinica, 2007, 43: 113−118. (in Chinese)

[34] GRÖBNER J, MIRKOVIC D, OHNO M, SCHMID F R. Experimental investigation and thermodynamic calculation of binary Mg−Mn phase equilibria [J]. Journal of Phase Equilibria and Diffusion, 2005, 26: 234−239.

采用金属/气体共晶定向凝固法制备藕状多孔 Mg−Mn 合金

周灿旭[1]，刘 源[1,2]，张华伟[1,2]，陈 祥[1,2]，李言祥[1,2]

1. 清华大学 材料学院，北京 100084；

2. 清华大学 先进成形制造教育部重点实验室，北京 100084

摘 要：采用金属/气体共晶定向凝固工艺(Gasar 工艺)制备藕状多孔 Mg−*x*Mn(*x*=0，1，2，3，质量分数，%)合金。研究 Mn 含量以及工艺参数对多孔镁锰合金孔隙率、孔径和显微组织的影响。结果表明，Mn 的加入促进含 Mn 析出相的形成，并提高材料的孔隙率和孔径。随着氢气压力从 0.1 MPa 增加到 0.6 MPa，Mg−2%Mn(质量分数)铸锭的体孔隙率从 55.3%下降到 38.4%，平均孔径从 2465 μm 下降到 312 μm。通过理论模型计算不同氢气压力条件下制备的铸锭体孔隙率，预测结果与实验结果吻合较好。因此，采用 Gasar 工艺可以制备出均匀且孔结构可控的藕状多孔镁锰合金。

关键词：多孔材料；Mg−Mn 合金；孔隙率；Gasar 工艺；定向凝固

(Edited by Bing YANG)